Proceedings of ASME Turbo Expo 2011
GT2011
June 6-10, 2011, Vancouver, British Columbia, Canada

GT2011-45282

SPRAY AND FLAME STRUCTURE OF A GENERIC INJECTOR AT AEROENGINE CONDITIONS

Ulrich Meier, Johannes Heinze, Stefan Freitag, Christoph Hassa
German Aerospace Center (DLR), Institute of Propulsion Technology
51147 Köln, Germany

ABSTRACT

In support of the development of CFD for aeroengine combustion, quantitative measurements of spray properties and temperature were made. A generic swirling air blast injector was designed and built to produce well defined inlet conditions and for ease of numerical description for the CFD development. The measurements were performed in an optically accessible single sector combustor at pressures of 4 and 10 bar and preheat temperatures of 550 and 650 K, respectively. Jet A-1 was used as fuel. The burner air to fuel ratio was 20 and the pressure loss was set to 3%. Sauter mean diameter (SMD) profiles and liquid mass flux distributions were generated from the phase Doppler anemometry (PDA) measurements of the evaporating spray drop sizes and velocities. With planar measurements of Mie scattering and kerosene-LIF, the distribution of kerosene (liquid and vapor phase) was imaged. Temperatures were measured with OH-LIF. The burner was designed with a straight outlet to exhibit lifted flames. Hence initial distributions of size, velocity and density of the spray were measured before it entered the flame. Almost complete prevaporization was seen at least for the 4 bar flame. Compared with atmospheric investigations, the smaller diameters of the droplets and the small streamline curvature of the configuration led to a more uniform behavior of the spray.

NOMENCLATURE

A_{eff}	Effective burner area
AFR	air-to-fuel ratio
D_{10}	Droplet diameter
D_{32}	Sauter Mean Diameter (SMD)
FWHM	Full Width at Half Maximum
L	combustor loading parameter
$\dot{m}$	combustor air mass flow
p	combustor pressure
(P)LIF	(Planar) laser induced fluorescence
SNR	signal/noise ratio
SSC	Single Sector Combustor
v_{mean}	mean droplet velocity
V	combustor volume

INTRODUCTION

Fuel preparation plays a crucial role in almost all aspects of aeroengine combustion. At high power, low NO_x emission depends on the quick mixing and homogenization of the fuel for both combustor concepts – RQL (Rich burn – Quick mix – Lean burn) and lean - that are in development today. At low power, it is decisive for the operability of the combustor to match the fuel placement with both the ignition source and the aerodynamic stabilization zone, and to achieve high vaporization rates. Computational tools are used to decrease the development time needed to satisfy all these demands and lower the costs of new combustion systems. Therefore efforts are undertaken to enhance the predictive quality of combustion CFD.

Validation data are required at every step of the CFD code development. This contribution reports some results of an experiment created to describe spray and combustion as completely as possible at realistic operating conditions. Only optical techniques are able to supply the necessary information, which calls for an optically accessible combustor. As yet there exist no computational methods to accurately model the atomization at realistic conditions, hence initial conditions of the spray have to be measured to enable validation of dispersion, evaporation and combustion.

For well defined starting conditions of the spray and ease of measurement, a generic atomizer was built, that had to be near enough to practical designs to be relevant. Special care was taken to enable the application of quantitative techniques for the measurement of the two-phase flow and temperature. As the air pressure influences the droplet size produced by air blast atomizers, the experiments need to be carried out above atmospheric pressure and with an amount of air preheat to induce evaporation rates similar to the engine.

This work is a continuation of a validation case carried out in the same combustor with a nozzle for natural gas with similar aerodynamics and a low speed fuel injection in an annular slot; this configuration mimicked to some degree the mixing process of an airblasted spray [1]. That experiment allowed the application of spontaneous Raman scattering to measure major species and temperature simultaneously, as well as the interaction of the swirling flow field with mixing jets typical of RQL combustors. Therefore this experiment was simplified to a combustor primary zone and concentrated on the burner near field and the quantities that are mostly influenced by the liquid fuel.

An important part of this effort was devoted to liquid fuel flux measurements. The details of the measurement procedure and the initial conditions of the 4 bar case have been reported in [2]. More indirectly, the present investigation is also a continuation of previous work which used the method to describe an isothermal spray [3], the effects of higher fuel loading on the 2-phase flow [4] and a combusting spray without preheat [5,6], all with a generic swirling air blast atomizer operating at atmospheric pressure. Measurements with an industrial atomizer at higher pressure are reported in [7], but without the temperature measurement. Measurements of velocity and fuel drop sizes in a matrix combustor at elevated pressure were presented in [8]. The effects of the degree of prevaporization have been described by Beck et al. [9].

EXPERIMENTAL

Test rig

The tests were performed in the optically accessible high pressure Single Sector Combustor (SSC). This facility was described in detail in [7]. The combustion chamber is schematically shown in Fig. 1. It features a square cross section of 102 x 102 mm and a length of 264 mm. Electrically preheated compressed primary air – shown in yellow – was supplied to the plenum upstream from the combustion chamber through a sonic nozzle, which was used for metering the air mass flow. Additional preheated air was diverted from the primary air supply and guided to the windows for cooling. The rig can be operated with up to 1 kg/s primary air at a maximum temperature of 850K and 2 kg/s cooling air. The secondary air supply shown in the figure was not used in these experiments. Burner and window cooling air mass flows were both controlled by sonic nozzles; therefore, the ratio of the air flows was always constant during a test, regardless of the absolute burner air mass flow. The latter was a function of the variable operating parameters combustor pressure, injector pressure loss and air preheat temperature. According to the sonic nozzle

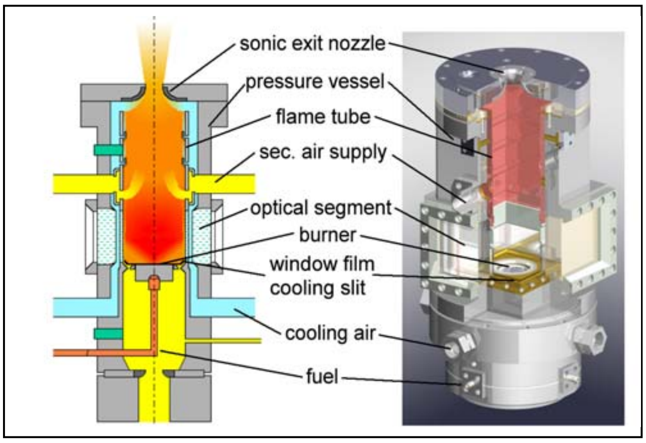

Fig. 1: Single Sector Combustor; left: schematic; right: 3D view

diameters (6.44 mm for burner air, 4 nozzles with 1.72 mm each for window cooling), the air mass flow ratios were: burner / window film = 1 / 0.285; in other words, the fraction of the total preheated air used for window cooling was 22%.

AFR (air/fuel ratio) values mentioned in this report refer to the burner air mass flow, not the total mass flow of preheated air. Although the amount of window cooling air was well defined, there was no way of knowing to which extent it mixed into the burner flow.

The combustor pressure was controlled by another sonic nozzle forming the choked exit of the combustor, along with additional cooling air (blue) which entered the flame tube just upstream from the exit, after cooling the outside of the windows in the optical section.

The entire rig was mounted on a three-axis traversing stage which allows positioning with respect to the measuring equipment with an accuracy of 0.1 mm. All planar measurements reported here were performed in a vertical plane through the centerline of the fuel injector, and – in the case of Mie scattering – in horizontal planes parallel to the burner faceplate.

Burner and test conditions

The burner was built for the purpose of generating a spray that was representative of aeroengine burners and at the same time had boundary conditions as well defined as possible. Pre-filming air blast atomization was chosen as the method of fuel injection, as it is most common in aeroengines. Two methods are typically used in industry to produce a film: A pressure swirl injector spraying on a swirl cup, or a film from an annular slot. Out of those, the latter method was chosen. The first method, although an elegant way to produce a circumferentially homogeneous film is very difficult to model, because the spray from the primary atomizer heats up before hitting the wall and many processes, that are difficult to describe or measure, happen in parallel before a film forms. For a film issuing from a circumferential slot, the calculation of the spray can then be started at the outlet of the fuel lines with the film or at the prefilmer lip with a semi-empirical atomization model, the initial measurements providing a first checkpoint of the calculation, or at the location of the measurements. Therefore the design of the burner was to provide a well defined fuel film with respect to temporal and spatial homogeneity as well as some information on temperature.

Figure 2 shows a schematic view of the generic burner, which was designed and manufactured at DLR, and some of its details. The design of the swirlers is shown in Fig. 3. The two air flows were co-rotating. Kerosene was supplied by two opposite fuel lines to an annular fuel gallery, and from there to a vertical slot through a circular array of 36 orifices with 0.2 mm^2 area each. The pressure drop across these metering holes, along with the length of the vertical slot, resulted in a good circumferential homogeneity of the fuel as it exited the end of the slot. The width of the annular slot was restricted to 0.5 mm to minimize the residence time of the fuel. At the end, the slot narrowed to 0.2 mm and was inclined at an angle of 31° which lead the fuel to the filmer lip with a radial momentum small enough to prevent it lifting from the filmer lip, see the detail on the upper right corner of Fig. 2. The purpose of the renewed constriction of the fuel path was the partial isolation of the coaxial fuel slot from the suction of the swirling air flow. Therefore the premature breakup of the film before the opening slot, which was observed in [10] for small film velocities, could be avoided. The filmer length was limited to 2 mm, because the aforementioned work [10] had shown atomization from the crests of the wavy film to develop at longer filmer lengths, whereas for the validation a well defined starting point of the fuel should be produced. The atomizer edge, see again the detail on the upper right corner, was made as thin as possible to prevent build up of liquid fuel mass in the wake of the edge, which could trigger discontinuous atomization. The angle of the edge was deduced from the angle of the inner contour of the outer swirler to have almost parallel airflows before atomization, such that the departing spray in the first phase of acceleration follows the direction of the inner contour.

As one result of these decisions, the thickness of the wall separating the air flow of the inner swirler from the fuel was rather thin, and as no other measures of thermal management exept reducing residence time were taken, a rather substantial heat up of the liquid fuel could be expected. This is known to influence atomization by lowering the surface tension of the fuel and accelerating evaporation rates by shortening the heat up time before the start of evaporation. Consequently, a calculation of the liquid phase will require a starting temperature. Therefore a thermocouple was embedded in the outer wall in the middle of the slot height to provide an estimate of the fuel temperature at the entry of the air channel.

Another consequence of the design was that optimum conditions for atomization were somewhat artificially produced at the expense of thermal management and airworthiness, which would not allow a slot height of 0.2 mm. In the absence of comparable measurements in industrial atomizers, it has to be assumed that the drop sizes produced were somewhat smaller than those from industrial configurations operating at the same conditions.

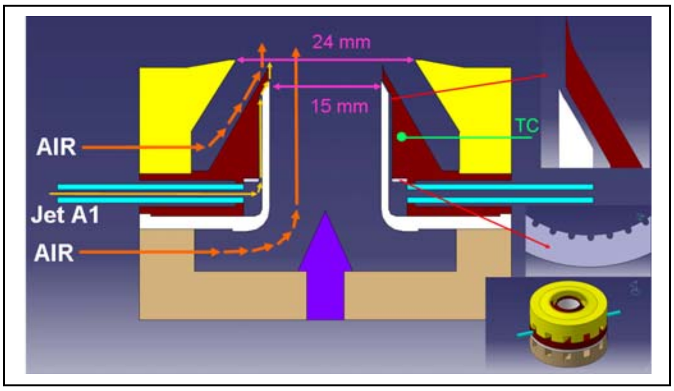

Fig. 2: Schematic of the burner; TC: Thermocouple

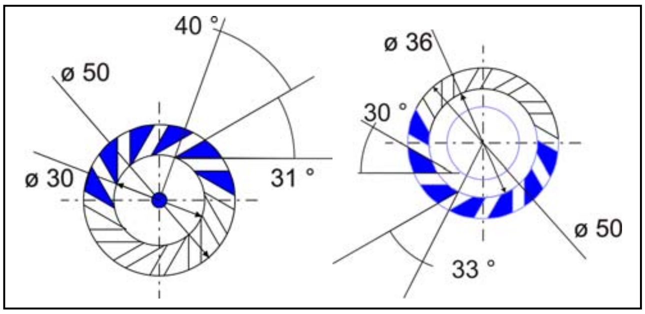

Fig. 3: Top view of details of the inner (left) and outer (right) swirlers

The diameter of the inner air channel of the injector was 15 mm; the exit diameter of the outer channel was 24 mm (see Fig. 2). The burner had an effective area of $A_{eff} = 242 \pm 1.8$ mm^2, as calculated from air mass flow, plenum pressure, burner pressure loss and preheat temperature.

The operating conditions for the test cases investigated are listed in Tab. 1. The first case A at low pressure and low preheat temperature is corresponding to idle conditions of an engine, whereas for case B the higher pressure and preheat temperature is closer to a cruise condition. In both cases the mixture was slightly lean; the stoichiometric AFR for kerosene is 14.7. Combustor loading parameters, defined as $L = \dot{m}/(V \cdot p^2)$, with V: combustor volume, are given as well. Velocity distributions were measured in the non-reacting case C.

For low pressure operation, it turned out that both combustor pressure and the spatially integrated OH chemiluminescence exhibited strong periodic oscillations with frequencies between 250 and 500 Hz if the pressure was reduced below 4 bar. An increase of the air temperature from 550 to 570 K resulted in a wall temperature rise from 450 to 460 K in the vertical fuel slot (see Fig. 2). Since the temperature measurement was not at the end of the fuel path, higher temperatures could be anticipated towards the filmer lip. Here, significant prevaporization could then take place, introducing instability in the fuel feed. More information about this effect is given in [11].

Test case		A	B	C
Air pressure p [MPa]		0.4	1.0	0.4
Air Preheat temperature T [K]		550	650	295
Burner pressure loss [%]		3	3	3
AFR burner [-]		20	20	-
Mass flux preheated air $\dot{m}$ [g/s]:	burner	60	140	82
	window film cooling	17	39	0
Loading parameter L [kg/(s*m^3*bar^2)]		1.72	0.65	-
Liquid fuel [g/s]		3.0	6.8	-

Tab. 1: List of test conditions

In any case, the tendency to exhibit instabilities is correlated with the fuel flow: Under conditions where the fuel flow is low, i.e., at low pressures and/or high AFR values, fluctuations occurred. Consequently, this limiting factor for the choice of operating conditions was less important at the higher pressure.

Diagnostic Techniques

In addition to video observation, the following measurement techniques were applied:

- OH chemiluminescence with Abel inversion [12] for visualization of reaction zones in a plane through the burner axis;
- Planar Mie scattering for imaging of the liquid fuel phase;
- Planar laser-induced fluorescence (PLIF) of kerosene for imaging of both vapor and liquid phase of the fuel;
- PLIF of OH for visualization of mixing and determination of temperature distributions in lean regions of the flame;
- Phase Doppler Anemometry (PDA) for spray analysis: Droplet velocities, sizes, size distributions and volume fluxes;
- Laser Doppler Anemometry (LDA) for measurement of the isothermal flow field

More information on spectroscopic methods and their application in combustor test rigs can be found in [7, 13, 14]. The simultaneous laser absorption, kerosene and OH PLIF measurements allowed the correction of the PLIF images with respect to laser absorption. The absorption measurements are also the basis for a calibration of the OH PLIF images in terms of absolute OH concentrations. In lean flames and under the assumption of OH being in chemical equilibrium, temperatures can be inferred from OH concentrations. The uncertainty of the local OH concentration is less than 30%, mainly caused by the uncertainty of the fluorescence quantum yield for the unknown local gas composition. This [OH] uncertainty results in an uncertainty of the temperatures of 40K - 65K in lean flames [15]. Moreover, the assumption of chemical equilibrium is violated in the reaction zone. The OH superequilibrium concentration within the flame front leads to an overestimation of the temperature of about 100K, but the relaxation takes place within less than 50µs at 10 bar [15].

We considered performing LDA measurements in the flame by seeding the air flow with titanium dioxide particles. It was found that in large regions of the flow there was a considerable contribution to LDA data rates by relatively big droplets, which could not be trusted to follow the air flow and hence would falsify the velocity measurements. This result led to the decision to restrict velocity measurements to the non-reacting conditions of case “C” in Tab. 1. The LDA measurements were performed by seeding the room temperature air flow with paraffin droplets generated by a droplet generator using an in-house design.

The accuracy of an LDA measurement was governed by the parameters listed in Tab. 2. As an example, for a typical LDA measurement with a mean velocity of v_{mean} = 49.8 m/s, with a confidence level of 99%, a width of the velocity probability distribution of 18.9 m/s and 20 000 validated samples, the resulting confidence interval for v_{mean} was 49.6 m/s – 50.14 m/s.

	LDA	PDA velocity for D_{10}=2µm	PDA D_{32}
beam separation (%)	±0.4	±0.4	±0.4
processor accuracy @ 0 dB SNR (%)	±0.5	±0.5	±0.5
discretization (%)	±0.01	±0.13	±0.13
val. sample size (-)	20 000	150	50 000
conf. level (%)	99	95	99
distribution width	18.9 m/s	20.5 m/s	5.49 µm
v_{mean} (m/s)	49.8	55.7	-
$D_{10,mean}$ (µm)	-	-	10.67
Confidence interval	**49.6-50.14 m/s**	**52.3-59.0 m/s**	**10.61-10.73 µm**

Tab. 2: Error sources, validated sample sizes and typical resulting accuracies for LDA and PDA setups

The PDA setup used is described in detail in [2]. The optical setup, which employed an off-axis angle of the receiving optics at Brewster’s angle of 68°, allowed measurements of semi-traverses in radial direction at axial distances between 7 mm and 30 mm. These limitations resulted from either clipping of laser beams or obscuration of the receiving optics by the window frames in the pressure vessel. A 2D optic was used; therefore it was necessary to scan two radial traverses orthogonal to each other, in order to retrieve all three velocity components.

Error sources for PDA measurements were similar to those for LDA, see Tab. 2. For the PDA tests, the abort criterion was set to 50 000 validated samples. For the analysis of droplet velocities including all droplet sizes, this higher number lead to a smaller confidence interval as for the above mentioned LDA case. But for velocities of specific droplet sizes, the number of events was lower: For a drop size of 16µm, it was typically 3 000 samples and for a drop size of 2µm around 200 samples, respectively. For a 2µm ± 10% droplet size case with a very low number of 151 validated events, an axial mean velocity of v_{mean} = 55.7 m/s, a velocity distribution width of 20.5 m/s and a 95% confidence level, the confidence interval for v_{mean} was larger: 52.3 m/s - 59.0 m/s. For the droplet size itself, at 99% confidence level for a typical case with a mean droplet size of D_{10} = 10.67 µm, a probability distribution width of 5.49 µm and a number of 50 000 validated events, the confidence interval for D_{10} was 10.61 µm - 10.73 µm. The highest effect on droplet size accuracy was caused by the temperature fluctuation in the reaction zone, resulting in a variation of the refractive index. With the PDA alignment used, a temperature variation of 100K resulted in a change of 0.9% of the measured drop size.

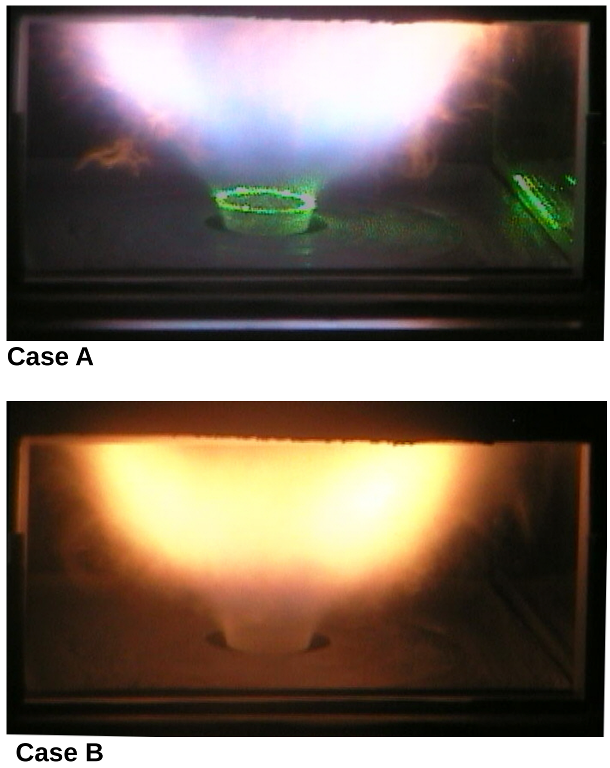

Fig. 4: Photographs of flame A (top) and B (bottom). Image of flame A shows also laser light sheet for fuel imaging by Mie scattering

RESULTS

Flame Structure

The visible appearance of flames A and B is shown in Fig. 4. The pictures are still images extracted from video recordings of a surveillance camera. The recordings were made with an auto-iris lens; therefore, images cannot be compared in terms of brightness.

With increasing pressure the color changes from blue-white to the characteristic bright orange-yellow, indicating increased soot production. The fuel spray cone is visible between burner exit and the upstream edge of the flame. The annular shaped green structure in the image of flame A in Fig. 4 is scattered light from a horizontal laser light sheet, which illuminated the spray cone for fuel imaging by planar Mie scattering.

Both flames were lifted. The average liftoff distances can be determined from OH chemiluminescence images. Fig. 5 shows Abel-transformed images of the reaction zones for both flames, with the liquid fuel distribution superimposed as contour plot. The contour lines indicate 10%, 20%, and 50%, respectively, of the maximum in the corresponding fuel distribution image. The intensity ranges for the false color plots are different for clarity, and hence not comparable between the images. OH chemiluminescence can be regarded as a reasonable qualitative indicator for reaction zones, but is no quantitative measure for the heat release, since it depends in general on more parameters than just heat release in turbulent flames. Hence, no quantitative scale can be assigned to the images.

Strictly, the Abel transform algorithm is applicable only to objects with cylindrical symmetry, which was not necessarily given here due to the quadratic contour of the combustion chamber. However, as can be seen in Figs. 8 and 10, the radial extension of both fuel and air flow was small compared to the combustor size of 102 x 102 mm; furthermore, the heat release regions were located close to the fuel flow, which was proven to be axisymmetric by planar Mie scattering in a plane parallel to the burner exit plane. Therefore, the assumption of axial symmetry of the flow was justified.

For both flames, the region of highest heat release was clearly downstream from the fuel, but the distance was substantially larger for flame A. The separation between fuel and heat release was much sharper at lower pressure. However, the observation of an apparent overlap between liquid fuel and heat release distributions at 10 bar is misleading. Both quantities are time-averaged, so high spatial fluctuations are actually more likely the reason for this “average” overlap, whereas instantaneous images would show well-separated heat release and fuel structures. Such high fluctuations of the fuel

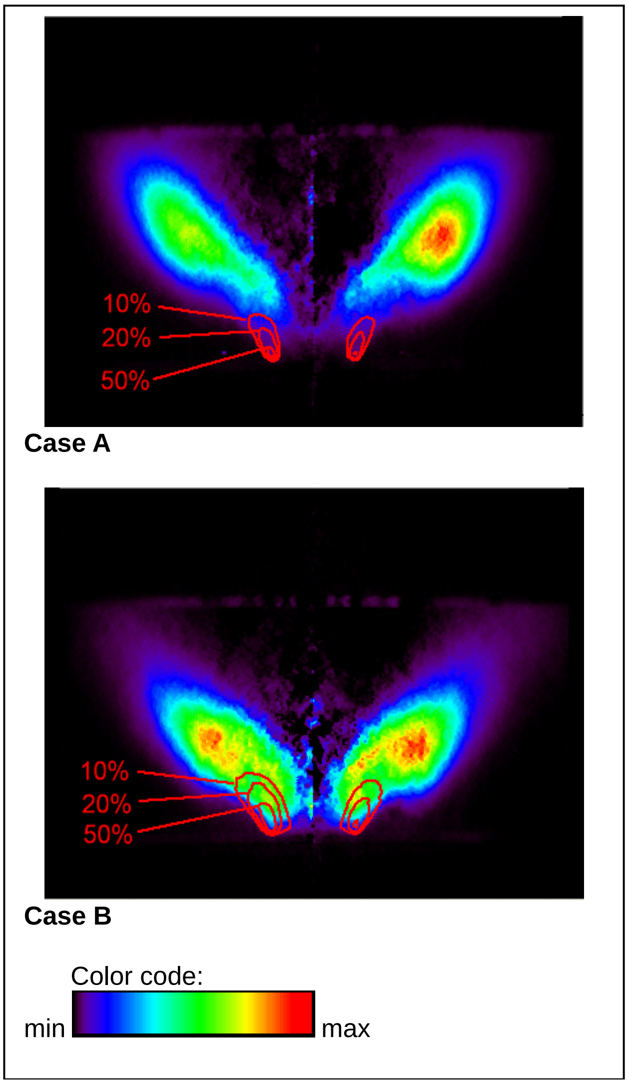

Fig. 5: Heat release (false colour) and liquid kerosene distribution (contour) for flames A (top) and B (bottom). See text for explanation of false colour scale. Contour lines are at 10%, 20 %, and 50% of maximum intensity

distribution were actually observed on a single laser pulse basis. This is illustrated in Fig. 6, where two instantaneous images of the temperature are shown for case B, with the distribution of the fuel (liquid and gaseous) superimposed as contour. The contour line indicates the region where the PLIF signal of kerosene has dropped to 10% of its maximum in the respective image. Both images show regions with steep gradients of the temperature, which indicate the flame front, and large diffuse areas with intermediate temperatures, which are typical for recirculation zones. The regions with unburnt mixtures where the equivalence ratio is too high to establish flammability conditions are visible inside the fuel contour lines. Reaction fronts are found in regions upstream of the penetration length of the fuel, which exhibits a large pulse-to-

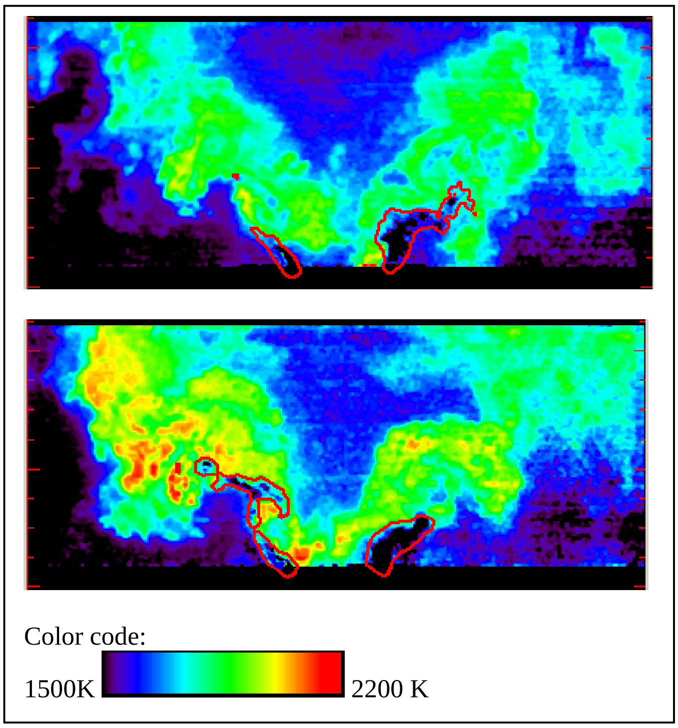

Fig. 6: Examples of instantaneous distributions of temperature and fuel. Test case B: p=10 bar, T=650 K, AFR 20. Contour line indicates 10% of initial fuel PLIF signal

pulse fluctuation; this results in an apparent overlap of fuel and heat release when images are temporally averaged.

In both cases in Fig. 5, reactions take place predominantly along the inner surface of the spray cone, where high temperatures, resulting from an inner recirculation zone, promote combustion.

The effect of operating conditions on flame liftoff can be seen more quantitatively in Fig. 7, which shows axial profiles

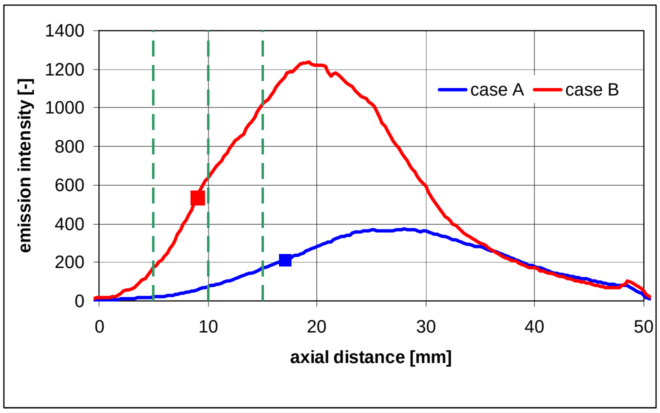

Fig. 7: Axial distributions of heat release along burner centerline. Green lines indicate measurement positions of radial profiles of spray distributions. Liftoff distances are marked with square symbols

of the OH chemiluminescence intensity along the centerline of the burner. For these profiles, the raw images of line-of-sight-integrated OH* emission, i.e. without Abel inversion, were evaluated. The vertical dashed lines at 5, 10 and 15 mm axial distance indicate the axial locations of the measurement planes for the radial distributions of liquid kerosene. Although the flames show no sharp distinct onset of heat release on average, the figure gives an idea of the individual liftoff distances. In particular, the large liftoff distance for flame A at 4 bar, visible qualitatively already in Fig. 5, is confirmed. If the axial position of the steepest gradient of the increasing UV emission intensity is defined as liftoff distance, the values are 17 mm for case A and 9 mm for case B, respectively. These coordinates are marked with squares.

The progress of spray dispersion and evaporation with increasing axial distance can be seen in Fig. 8, which shows profiles through distributions measured by planar Mie scattering in a plane parallel to the burner faceplate (see top image in Fig. 4 for orientation) for flames A and B. The table below the diagrams gives the peak-to-peak diameter of the spray cone, as well as the full width at half maximum (FWHM), averaged over both peaks at each axial location. For comparison, the diameter of the fuel exit slot in the burner was 15 mm. The profiles are very similar for flames A and B; in particular the radial spread is identical for both flames, while the spray cone thickness is slightly higher for case B. This suggests that there was only a small influence of pressure on fuel patternation for the flow field of this burner.

Figure 9 summarizes time-averaged distributions of liquid fuel, liquid + vaporized fuel, heat release, and temperature, respectively, in a plane through the centerline of the burner for both flames. The image area is 105 mm x 80 mm. The planar heat release distribution was reconstructed from line-of-sight-integrated OH* chemiluminescence images using an inverse Abel transform algorithm [12]. Temperatures were calculated from absolute OH densities, which were in turn measured by simultaneous PLIF and absorption. Details of this method are described in [15]. Due to the rapidly decreasing OH concentrations with temperature, the lower temperature limit accessible by this method was approximately 1500 K. Correspondingly, the color bar for the temperature images covers the range from 1500 to 2200 K.

As a consequence of this temperature range limitation, measurements in regions with high temporal fluctuations and frequent occurrence of low temperatures were affected by a systematic bias towards high temperatures. This was typically the case in mixing regions of burnt and unburnt mixtures. The bias resulted from the fact that the low temperatures in the probability distribution were not captured by the measurements. Since the shape of the temperature PDF was unknown, the resulting error could not be quantified; however, the regions in the temperature distribution where this bias occurred can be identified by a statistical evaluation of the instantaneous temperature measurements at each location. For the situation reported here, only the areas with the lowest

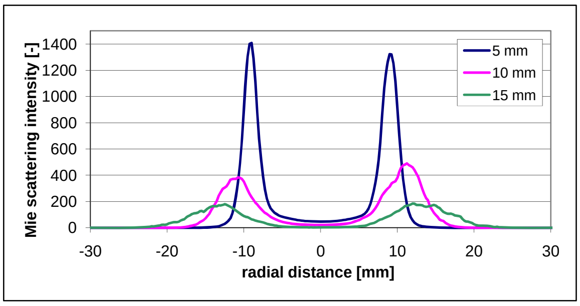

Case A	diameter (max-max) mm	FWHM mm
5mm	18.0	2.38
10mm	22.0	5.25
15mm	24.5	8.12

Case A

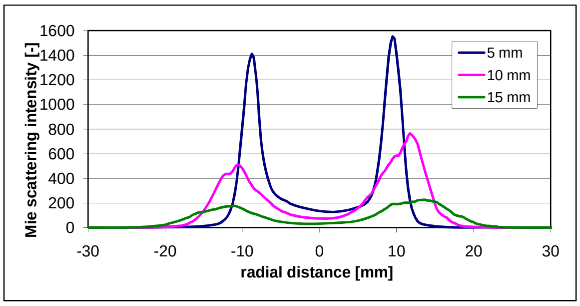

Case B	diameter (max-max) mm	FWHM mm
5mm	18.5	2.75
10mm	22.0	6.50
15mm	24.5	9.60

Case B

Fig. 8: Radial profiles from cuts through planar distributions of liquid fuel in a plane parallel to burner exit at three different axial positions

temperatures at large radial positions and approximately 10 mm or less axial distance, i.e., in the region of the outer recirculation zone, were affected by this bias. Regions with constantly sufficiently high temperatures, like the reaction zones or the inner recirculation zone, were not affected.

The relative intensities for each measured quantity are comparable for both flames. The white horizontal line in each image indicates the location of the burner exit plane. A downstream bent edge of the burner heat shield, which served as guide vane for the window cooling air, obscured the lower edge of the light sheet and prevented measurements down to the burner exit plane.

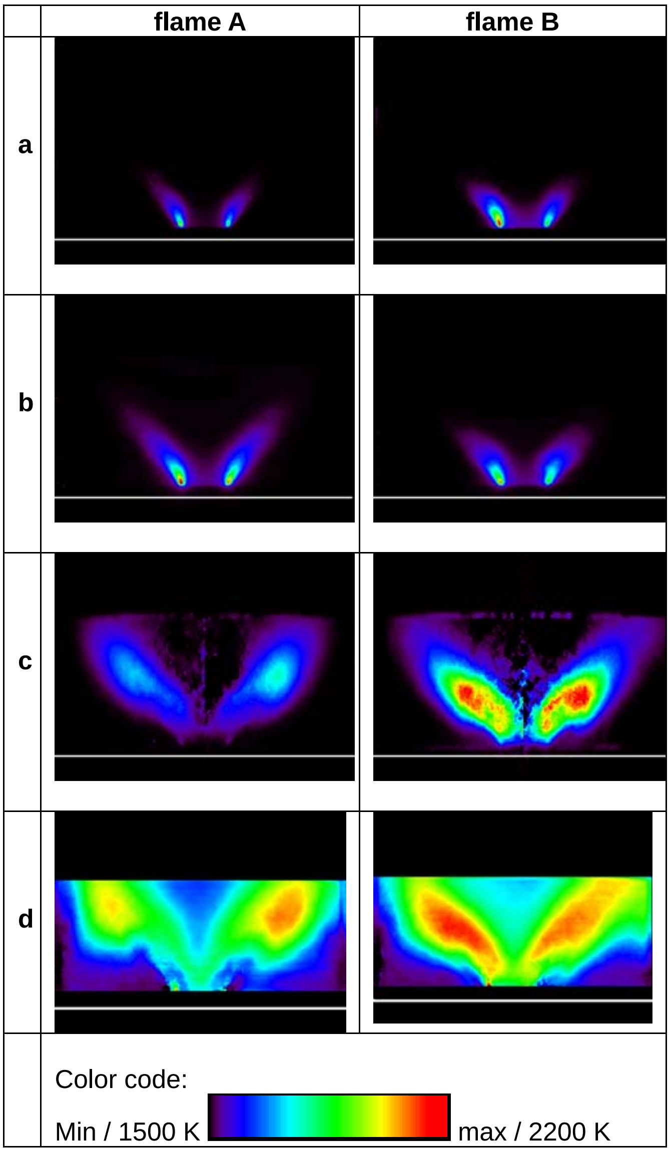

Fig. 9: Spatial distributions in central plane of liquid fuel (a), liquid and gaseous fuel (b), heat release (c), and temperature (d) for flames A and B. White line indicates burner exit plane

Despite the higher preheat temperature and pressure in case B, there was hardly any difference in the spray penetration depth between the two flames, although both atomization and evaporation should be faster for flame B. This was apparently offset by the higher fuel mass flow. However, due to the accelerated fuel consumption rate at higher temperature and pressure, the penetration of the vapor phase fuel decreased, and the reaction zone shifted closer to the burner. The temperature images in row d of Fig. 9 show a faster rise in axial direction for flame B. Furthermore, a comparison of the reaction zone images (c) and the temperatures (d) suggest the existence of an inner recirculation zone, with high temperatures near the centerline although no reactions take place there.

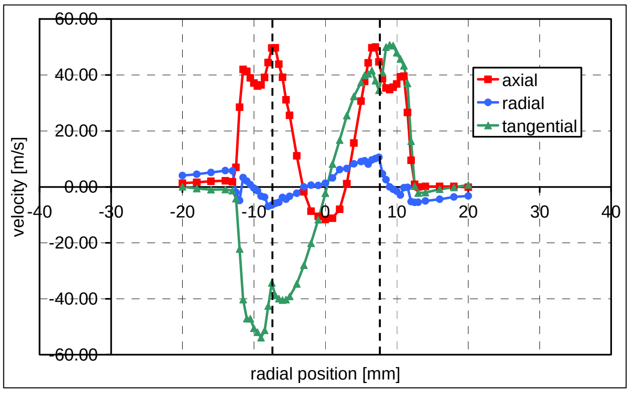

Fig. 10: Radial velocity profiles in isothermal flow, case C

This inner recirculation is clearly visible in the radial velocity profiles of the isothermal flow shown in Fig. 10. The profiles were measured at an axial distance of 2 mm from the burner exit plane. The dashed vertical lines at +/-7.5 mm radial distance indicate the diameter of the inner air channel, see Fig. 2. The small dips visible in the peaks of the axial and tangential velocity indicate the wake of the prefilmer lip. The swirling flow resulted in an outward bound radial motion up to the position of the prefilmer. Outside the fuel feed annulus, the radial component reversed its sign because the flow was forced inward by the contour of the outer air channel. At larger radial distances, beyond the outer edge of the outer air channel, the radial component remained negative, due to a weak outer recirculation zone.

The following diagrams summarize the results of the PDA measurements. Figure 11 shows the liquid volume flux and the droplet velocity field in a plane through the burner axis for case A. It is evident that the flow pattern is in good agreement with the orientation of the fuel flux distribution. The flux data were integrated along the circumference to yield a total volume flow. This volume (or mass) flow was checked against the input kerosene mass flow obtained from rig data and was found to be consistent at axial distances beyond 10 mm. Closer to the burner, the PDA processor turned out to be saturated due to high data rates resulting from dense spray [2].

The fuel flux along the “center of mass”, i.e. the central part of the distribution, starts to decrease rapidly at axial distances above 15 to 20 mm, which is consistent with the liftoff distance of the flame, as shown in Fig. 7; however, there is still liquid fuel in the region with high heat release. Again, as mentioned in the discussion of Fig. 5, this may be a result of averaging over large temporal and spatial fluctuations of heat release and/or fuel distributions, which could not be captured in the measurements shown here. For 10 bar, the spray was so dense, that with 20%, the fraction of the captured mass was not big enough to allow a quantitative representation.

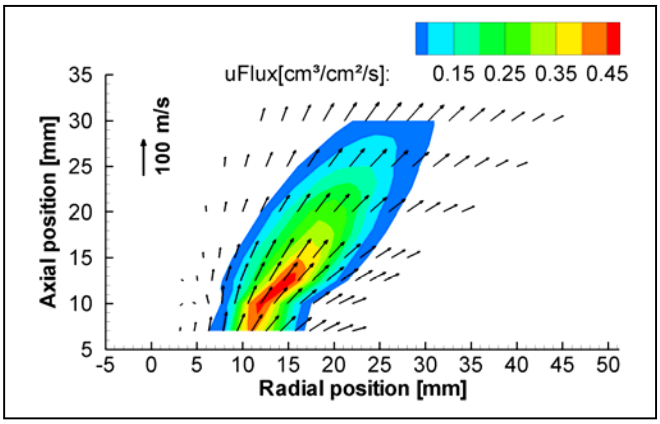

Fig. 11: Volume flux (false color) and velocities for droplets with size 16 µm +/- 10%, case A

Figure 12 compares velocities for particles with different sizes. The 2µm droplets can be taken as reasonable approximation of the gas velocity, whereas the 16 µm droplets are an approximation of the global Sauter Mean Diameter D_{32}, see Fig. 15. Therefore, Fig. 12 also describes to some extent the relative motion of the spray. The spray was accelerated up to the measurement location at 15 mm. Downstream of that line, combustion started gradually, consuming first the smallest droplets such that not enough droplets of the small size class were measured to give a good statistical average of the gas flow. The swirling air jet spreaded outward and therefore widened and decelerated up to an axial distance of 20 mm. After that line, the heat release with the ensuing rarefaction and acceleration of the gas flow counteracted the foregoing effects just enough to result in the constant velocities of the remaining droplets, as shown in Fig. 13. The higher inertia of the bigger droplets lead to higher radial velocities throughout the forward flow, as the droplets having picked up tangential velocity also

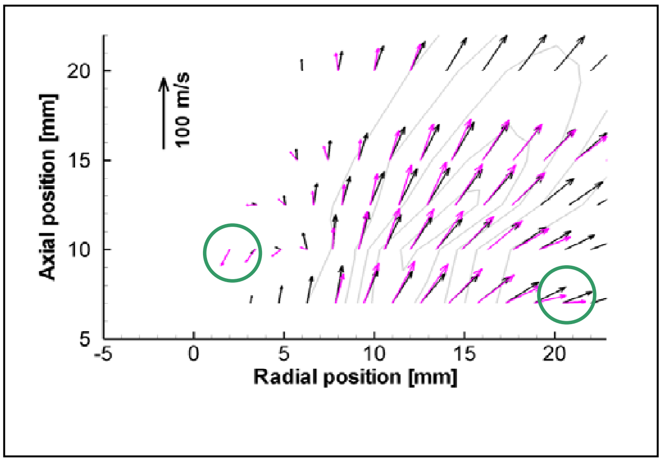

Fig. 12: Droplet velocities for particles with size 16 µm +/- 10% (black) and 2 µm +/- 10% (red), case A

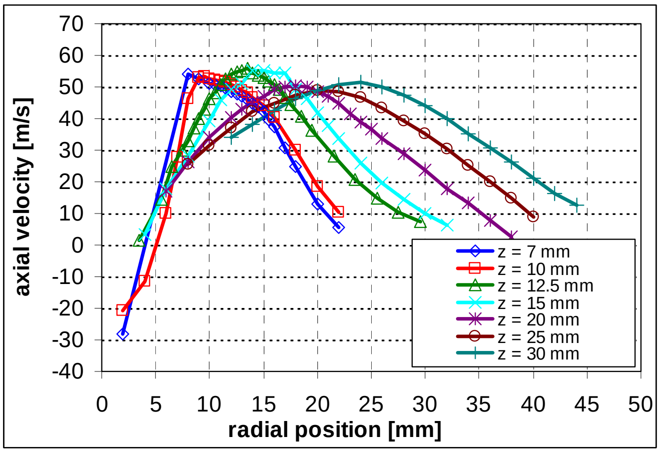

Fig. 13: Radial profiles of axial velocity component at different axial positions z for case a. All particle sizes are included.

experience centrifugal forces. Consequently this effect was more marked for smaller radii. At the shear to the outer recirculation, the big droplets had a velocity overshoot, which caused their direction to be slightly more inward than the gas flow. However, the trajectories for 16 µm and 2 µm droplets were similar, indicating little separation – which will be confirmed by the following results. This is a remarkable difference to well known trends of atmospheric investigations, where big droplets are often seen to be centrifuged out of the jet, see for example Ref. [4]. The first reason that comes to mind is the different Stokes number of the droplets due to the differences in size and density ratio. However it should be also kept in mind that this configuration deliberately had slower radial gas movement as most industrial configurations, because a lifted flame was intended, that in fact did allow to measure initial conditions which are not too much influenced by the flame.

A more quantitative representation of the weak size separation is given in Fig. 14, which shows radial profiles of the axial velocity component at an axial position of 7 mm for four size classes. The velocities were generally very similar, with the largest differences occurring at radial positions between 8 and 15 mm, which was the region with the highest spray density (see Fig. 11). It should be mentioned that at this axial position the acceleration phase of the droplets was already completed.

Bigger differences become visible at the points marked by green circles in Fig. 12. Small droplets entered the inner and outer recirculation already identified by the isothermal measurement.

Sauter mean diameters of kerosene droplets are shown for both test conditions and different axial positions in Fig. 15. In the region of the core of the fuel flow, at radial distances between 10 and 20 mm, only a small decrease of D_{32} was observed with increasing distance for both pressures; also

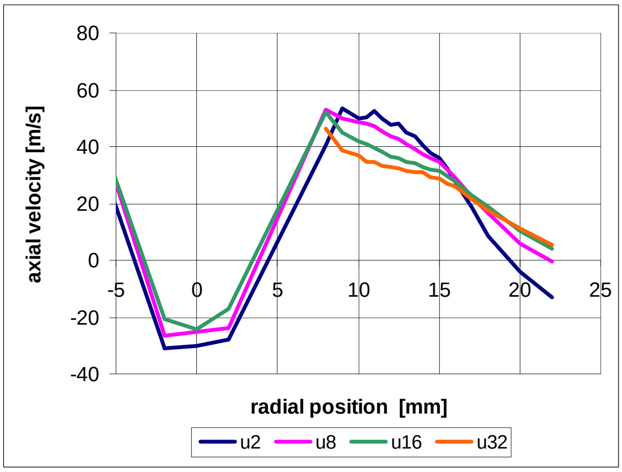

Fig 14: Case A: Profiles of axial velocities at axial position 7 mm for different size classes: 2 µm (u2), 8 µm (u8). 16 µm (u16), and 32 µm (u32); width of each size class ±10% of central size

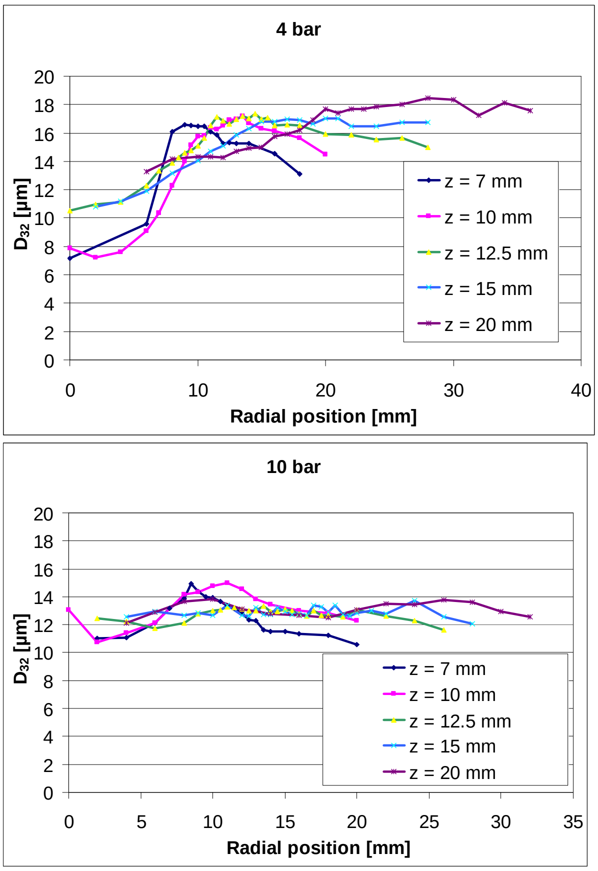

Fig. 15: Radial profiles of SMD at different axial positions z for case A (top) and B (bottom)

radial variations were relatively small except in the region below 8 mm in case A. Here, the small droplet sizes, particularly at 7 and 10 mm axial distance, resulted from the capture of only small droplets by the inner recirculation zone, as shown also Figs. 12 and 13. This effect is visible also at 10 bar, although to a lesser extent. At the largest axial distances in case A, the faster radial movement of the bigger drops lead to an increase of D_{32} from about 14 to 18 µm, while in case B, D_{32} remained almost constant, due to the smaller droplet size and the lower density ratio at higher air pressure.

This observation is illustrated more clearly in Fig. 16, which shows a comparison of radial profiles of D_{32} at 15 mm axial distance for cases A and B. D_{32} values for case B were generally smaller than for case A, due to the atomization and evaporation associated with higher pressure and preheat temperature. This provides some justification for their presentation despite the fact, that the full spray volume was not captured. The sensitivity of the sizes measurement was not so severely impaired, that the lower diameters produced by the atomization at higher pressure could not be recorded.

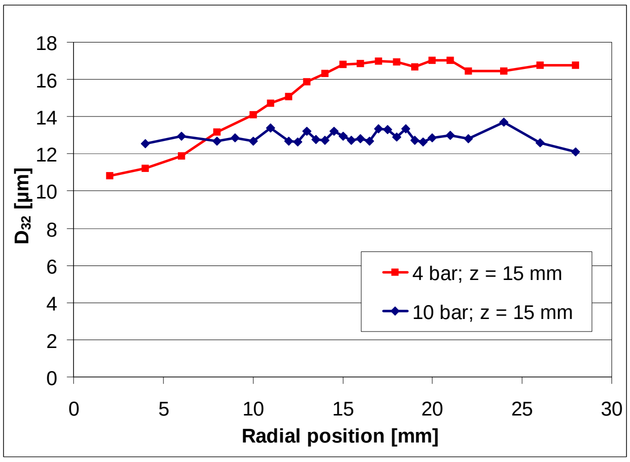

Fig. 16: Radial distributions of SMD for case A (red) and B (blue) at axial distance z = 15 mm

CONCLUSIONS

Quantitative measurements of temperature, droplet velocity, sizes and liquid fuel flux were performed for an air blast atomizer at elevated pressure. To our knowledge, this represents an increase in the operating range in terms of reacting high pressure two-phase flows in combustion chambers, where quantitative data are available. Planar measurements of the heat release by OH chemiluminescence imaging, Mie scattering, and kerosene PLIF imaging revealed the relationship between fuel placement, reaction zones, and resulting temperature distributions.

Compared to the structure of a swirling spray with an inner recirculation zone known from atmospheric experiments [5], the current data show much less relative movement of the spray and therefore less separation of bigger and smaller droplets.

The effect is clear at 4 bar but even more pronounced for 10 bar. The implications for the modeling of combusting two phase flows in aeroengines are potentially important, therefore the relevance of this result needs to be put into perspective. For the goal of a clean validation case with well defined starting conditions and good circumferential homogeneity, some liberties were taken in the design of the injector, that are not airworthy or practical for mass production. Their probable consequence is a lower mean diameter but also, as a result of circumferential homogeneity, a lower amount of big droplets. So size measurements and size velocity correlations of practical atomizers at medium pressure are needed, even if volume flux measurements turn out to be too difficult, as the next step of validation. However, since medium pressures of large aeroengines, e.g. at cruise, will be higher than the pressures investigated here, a similar drop size level can be expected at those pressures. Furthermore, the gas flow field had little streamline curvature, which makes it easier even for the bigger droplets to follow the flow. Fitting a diffuser to the current injector, thereby creating a faster spread of the swirling flow and a stronger inner recirculation zone would be more typical for the current combustors with short primary ones and might change the picture.

With regard to mixing and homogenization, a compact droplet size distribution with small droplets can be a mixed blessing. Although the droplets react better to turbulence on the small scales, less droplet slip reduces the radial dispersion and with it the dilution of the spray, that goes with the radial movement of the spray. Such an effect has been observed in an isothermal swirling flow with jet in cross flow atomization with higher pressures [9]. That notwithstanding, larger drop sizes are not desired, as a bigger gain towards better operability can be achieved at low power with the lowest possible drop size.

The complete set of measurements is intended to serve as a comprehensive validation data base for development and test of CFD tools.

Future work on this case will focus on the unsteady aspects of the flow that will enhance the statistical analysis of the data.

ACKNOWLEDGMENTS

This work received funding from the European Community through the project TIMECOP-AE (Project # AST5-CT-2006-030828). It reflects only the author's views and the Community is not liable for any use that may be made of the information contained therein.

REFERENCES

[1] Hassa, C., Willert, Ch., Fischer, M., Stockhausen, G., Röhle, I., Meier, W., Wehr, L., and Kutne P., 2006, “Nonintrusive Flowfield Temperature and Species Measurements on a Generic Aeroengine Combustor at Elevated Pressures”, Proc. ASME Turbo Expo, ASME-GT-90213.

[2] Freitag, S., Meier, U., Heinze, J., Behrendt, T., and Hassa, C., 2010, „Measurement of Initial Conditions of a Kerosene Spray from a Generic Aeroengine Injector at Elevated Pressure”, Proc. 23rd Annual Conference on Liquid Atomization and Spray Systems (ILASS-Europe 2010), Brno, Czech Republic , 6.-8.Sept. 2010, Paper No. 137, ISBN-978-80-7399-997-1.

[3] Hassa, C., Blümcke, E., Brandt, M., and Eickhoff, H., 1992, “Experimental and Theoretical Investigation of a Research Atomizer/Combustion Chamber Configuration”, ASME-GT-137, Köln.

[4] Brandt, M., Hassa, C., and Eickhoff, H., 1992, “An Experimental Study of Spray - Gasphase Interaction for a Co-Swirling Airblast Atomizer”, 8th. Annual Conference of the Institute of Liquid Atomisation and Spray (ILASS) Europe, Amsterdam.

[5] Hassa, C., Deick, A., and Eickhoff, H., 1993, “Investigation of the Two-Phase Flow in a Research Combustor under Reacting and Non-Reacting Conditions”, AGARD CPP-536: Fuels and Combustion Technology for Advanced Aircraft Engines.

[6] Ghaffarpour, M. and Chehroudi, B., 1993, “Experiments on Spray Combustion in a Gas Turbine Model Combustor”, Combustion Science and Technology, 92(1), pp. 173 – 200.

[7] Behrendt, T., Frodermann, M., Hassa, C., Heinze, J., Lehmann, B., and Stursberg K., 1998, „Optical Measurements of Spray Combustion in a Single Sector Combustor from a Practical Fuel Injector at Higher pressures”, RTO Applied Vehicle Technology Panel, Symp. on Gas Turbine Engine Combustion, Emissions and Alternative Fuels, Lisbon, 12.-16.Oct.

[8] Heath, C.M., Anderson, R.C., Hicks, Y.R., and Locke, R.J., 2010, “Optical Characterization of a Multipoint Lean Direct Injector for Gas Turbine Combustors: Velocity and Fuel Drop Size Measurements”, ASME-GT-2010-22960.

[9] Beck, C.H., Koch, R., and Bauer, H.-J., 2007, “Investigation of the effect of incomplete droplet prevaporization on NOx emissions in LDI combustion systems”, ASME-GT-27654.

[10] Bhayaraju, U., and Hassa, C., 2009, “Planar Liquid Sheet Breakup of Prefilming and Nonprefilming Atomizers at Elevated Pressures”; Atomization and Sprays 19(12), pp. 1147-1169.

[11] Hassa, C., Heinze, J., Meier, U., Heeger, C., Trunk, P., and Dreizler, A., 2010, „Self-Excited Oscillation in a

Combustion Chamber Driven by Phase Change in the Liquid Fuel Feed System“, Int’l. Summer School and Workshop on non-Normal and Nonlinear Effects in Aero- and Thermoacoustics, Munich, May 17-21.

[12] Dasch, C. J., 1992, “One-Dimensional Tomography: a Comparison of Abel, Onion-Peeling, and Filtered Backprojection Methods”, Applied Optics, 31(8), pp. 1146 -1152.

[13] Kohse-Höinghaus, K., and Jeffries, J.B., eds., 2002, „Applied Combustion Diagnostics“, Taylor & Francis, ISBN 1-56032-913-0.

[14] Meier, U.E., Wolff-Gassman, D., and Stricker, W., 2000, „LIF Imaging and 2D Temperature Mapping in a Model Combustor at Elevated Pressure”, Aerosp. Sci. Technol. 4, pp. 403-414.

[15] Meier, U., and Heinze, J., 2006, EU Project “TLC - Towards Lean Combustion”, Contract N°AST4-CT-2005-012326, Deliverable Report: D1.3.3.a: “Report on the description of the OH temperature measurement technique”.